Open Access

Colloidal PbS Quantum Dots for Visible-to-Near-Infrared Optical Internet of Things

Aigerim Tankimanova
Chun Hong Kang, *Graduate Student Member, IEEE*
Omar Alkhazragi, *Graduate Student Member, IEEE*
Haodong Tang
Meiwei Kong, *Member, IEEE*
Lutfan Sinatra
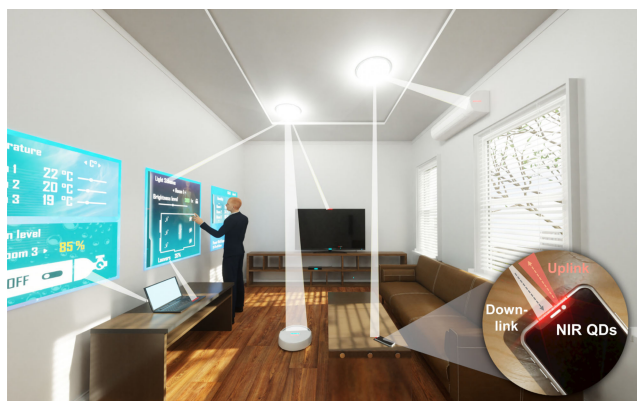Marat Lutfullin
Depeng Li
Shihao Ding
Bing Xu
Osman M. Bakr
Kai Wang, *Member, IEEE*
Xiaowei Sun, *Senior Member, IEEE*
Tien Khee Ng, *Senior Member, IEEE*
Boon S. Ooi

photonics SOCIETY

IEEE

Colloidal PbS Quantum Dots for Visible-to-Near-Infrared Optical Internet of Things

Aigerim Tankimanova,[1]
Chun Hong Kang (ID)**,**[1] *Graduate Student Member, IEEE*,
Omar Alkhazragi (ID)**,**[1] *Graduate Student Member, IEEE*,
Haodong Tang (ID)**,**[2] **Meiwei Kong** (ID)**,**[1] *Member, IEEE*, **Lutfan Sinatra,**[3]
Marat Lutfullin,[3] **Depeng Li,**[2] **Shihao Ding,**[2] **Bing Xu,**[2]
Osman M. Bakr,[4] **Kai Wang** (ID)**,**[2] *Member, IEEE*,
Xiaowei Sun (ID)**,**[2] *Senior Member, IEEE*,
Tien Khee Ng (ID)**,**[1] *Senior Member, IEEE*, **and Boon S. Ooi** (ID)[1]

[1]Photonics Laboratory, King Abdullah University of Science and Technology (KAUST), Thuwal 23955-6900, Saudi Arabia
[2]Guangdong University Key Lab for Advanced Quantum Dot Displays and Lighting, Shenzhen Key Laboratory for Advanced Quantum Dot Displays and Lighting, and Department of Electrical and Electronic Engineering, Southern University of Science and Technology, Shenzhen 518055, China
[3]Quantum Solutions LLC, Thuwal 23955-6900, Saudi Arabia
[4]Division of Physical Science and Engineering, King Abdullah University of Science and Technology (KAUST), Thuwal 23955-6900, Saudi Arabia

Abstract: The emergence of optical Internet of Things (optical-IoT) for sixth-generation (6G) networks has been envisaged to relieve the bandwidth congestion in the conventional radio frequency (RF) channel, and to support the ever-increasing number of smart devices. Among the plethora of device innovations deemed essential for fortifying the development, herein we report on the visible-to-near-infrared color-conversion luminescent-dyes based on lead sulphide quantum dots (PbS QDs), so as to achieve an eye-safe high-speed optical link. The solution-processed PbS QDs exhibited strong absorption in the visible range, radiative recombination lifetime of 6.4 μs, as well as high photoluminescence quantum yield of up to 88%. Our proof-of-principle demonstration based on an orthogonal frequency-division multiplexing (OFDM) modulation scheme established an infrared data transmission of 0.27 Mbit/s, readily supporting an indoor optical-IoT system, and shed light on the possibility for PbS-integrated transceivers in supporting remote access control of multiple nodes. We further envisaged that our investigations could find applications in future

development of solution-processable PbS-integrated luminescent fibers, concentrators, and waveguides for high-speed optical receivers.

Index Terms: Optical Internet of Things, quantum dots, lead sulphide, orthogonal frequency-division multiplexing.

1. Introduction

In the upcoming era of the Internet of Things (IoT), there is an ever-increasing demand for higher-speed, more power-efficient and secured data transmission to support various application scenarios. With the increasing number of handheld devices, the conventional radio frequency (RF) communication channel is expected to saturate in the near future [1], [2]. In order to resolve the bandwidth crunching issue in the RF technology, the optical wireless communication (OWC) technologies supplemented by the visible-light communication (VLC), operating in the 400-to-750-nm range of the electromagnetic spectrum, has long been envisaged to resolve these challenges [3]. The VLC or light-fidelity (Li-Fi) is aimed to address the overloading issue in the RF communication channels by utilizing indoor lighting as a hub for wireless data transmission points, in which it will create a bigger channel capacity in addition to the Wi-Fi technology [2], [3].

Although VLC is a promising technology for future indoor communications, there is a number of challenges that remain unresolved in the existing VLC or optical-IoT systems. One of such challenges is that high-speed photodetectors have small areas due to resistance-capacitance (RC) limits and so can only collect a small portion of the flux of photons, reducing the received signal power. Using a focusing element resolves this but limits the field of view, following the conservation of étendue, making the alignment requirements stricter. Thus, to reduce the chances of blocking of the optical signal, and to increase the amount of the received light, the receiver area should be of larger size, while, at the same time, not be limited by the RC limits, such as in the prior work by Peyronel *et al.* [4], in which the authors proposed a design of a flexible luminescent concentrator for free-space optical communication by utilizing optical fibers doped with visible fluorescent dyes. Similarly, in other works presented by Dong *et al.* [5] and Manousiadis *et al.* [6], fluorescent optical concentrators were aimed to increase the detection efficiency for the incoming visible-light signal, without degrading the field of view of the photodetectors. However, since these luminescent concentrators emit in the visible range, incorporating these materials into indoor optical-IoT systems will create undesirable illumination to the human eye in the long run under an indoor environment. In contrast, a luminescent dye emitting in the near-infrared (NIR) region, i.e., 750 nm to 2.5 μm, which allows the absorption of any incoming signals in the visible spectrum, is non-visible and visually non-disturbing to human vision, thus enabling a more conducive living environment empowered by the optical-IoT systems. Apart from the receiver end for downlink operation, the NIR luminescent dye could also be integrated on optical-IoT systems for uplink operation based on visible-light sources, i.e., display screens, and thus omit the costly development path of NIR-based vertical-cavity surface-emitting laser (VCSEL) arrays.

As illustrated in Fig. 1, an example of the incorporation of near-infrared dyes that can convert from the visible range, i.e., coming from the white light-emitting diodes (LEDs), to NIR can be implemented on the transceiver end for both downlink and uplink operation on various indoor smart devices, allowing remote access control over a vast variety of optical-IoT devices. Moreover, it is worth mentioning that unlike the abovementioned designs conceived for visible polymer-based waveguides having higher attenuation loss (i.e., 100 dB/km) [4]–[8], the NIR emitting color-converting element can be effectively coupled into matured silica-based optical waveguides that exhibit significantly lower losses (i.e., <1 dB/km) as compared to the visible range and thus it is further envisaged for integration into existing photonic integrated circuits (PIC). The silica-based optical fiber communication, operating in the NIR regime located at around 1300 nm and 1550 nm, is a relatively matured technology and had long been efficiently used for long-distance and high-speed data transmission due to low attenuation losses [9]. Moreover, the InGaAs-based photodetectors with the detection range of 900 nm to 1700 nm are typically
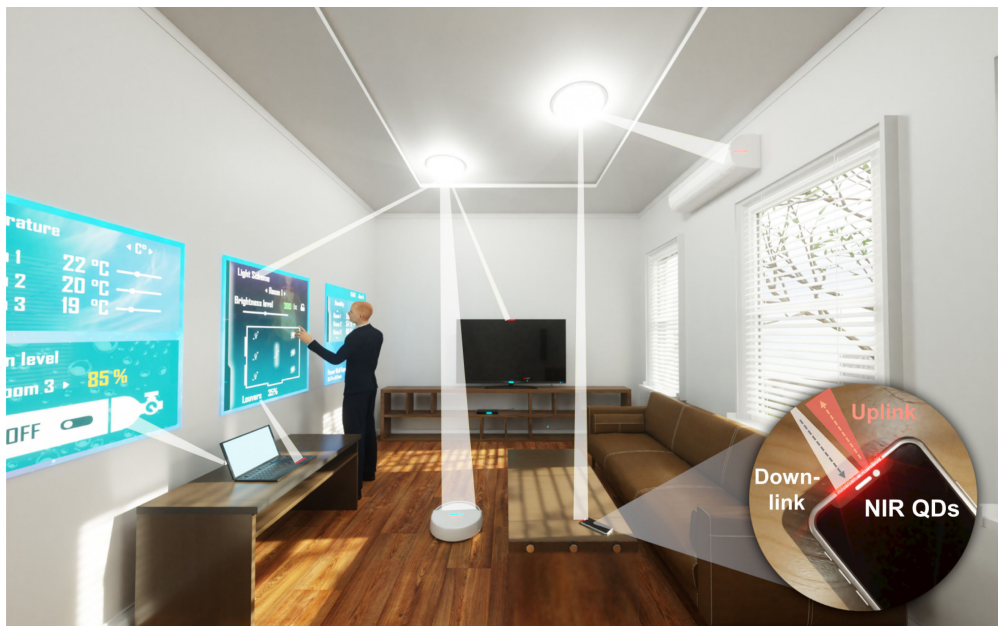
Fig. 1. Exemplary of near-infrared dye integrated at the transceiver ends to support various indoor optical-IoT systems requiring non-visual-interfering remote access control.

employed on the receiver end of the silica-based optical fiber communication for signal detection. Within the communication wavelengths of interest, the InGaAs-based photodetectors are known to have the highest responsivity and quantum efficiency as compared to other photodetectors, e.g., Si- and Ge-based photodetectors [9].

Although it is noted that, in the pursuit of expanding the detection range of InGaAs-based photodetectors up to the visible range, there have been several proposed solutions based on monolithic integration of different materials, such as by Geum *et al.* [10], where GaAs and InGaAs are used for visible and NIR photodetection, respectively. Likewise, in another work by Wang *et al.* [11], broadband detection was achieved by a GaSe/*n*-type GaSb heterostructure with the detection range of 400–1800 nm. Another interesting solution was proposed by Li *et al.* [12], where a broadband image sensor design was realized based on Zn_2SnO_4 nanowires covered by SnS QDs. However, it is important to note that these devices require cumbersome fabrication process techniques which are known to be cost- and process-intensive. Moreover, with the addition of said layers, the data rates of these devices were not investigated, and the low modulation bandwidth could possibly arise from intrinsic defects that might affect the overall response speed of the photodetectors.

Herein, in an effort to design an efficient VLC transceiver based on visible-to-NIR color-conversion that will broaden the detection spectrum of commercial InGaAs photodetectors, as well as for supporting the dual-functionalities of downlink and uplink operation, we aimed to utilize high-quantum-efficiency colloidal quantum dots (QDs), emitting in the near-infrared region, as the intermediate color-conversion medium in the communication links. The rapid advancements in nano-scale materials having low dimensional structures, e.g., quantum wells (QWs), nanowires (NWs), and QDs, have enabled a number of potential applications in the current market. Among all, the colloidal QDs are the most attractive due to the facile solution-based synthesis method and enhanced stability based on surface passivation [13]–[16]. Taking advantage of the stronger quantum confinement present in QDs, as compared to other low-dimensional structures, the development in this regard has enabled numerous applications in the field of optoelectronics, e.g., LEDs [13], [17] and photodetectors [13], [15], [18]. The inherent advantages of high quantum efficiency and short

lifetime present in colloidal QDs could potentially open up a plethora of opportunities in the field of high-speed OWC systems, such as the phosphor-based transmitter [19] and receiver modules [20] as demonstrated in our prior works. In this regard, the colloidal lead sulphide (PbS) QDs could be a promising candidate due to their broad absorption range from ultraviolet (UV) to NIR and possibility to control the emission wavelength in the NIR range simply by tuning the QDs diameters [21]. More-over, the solution-processed QDs can be easily integrated as the color-converting components by facile and standard fabrication techniques, e.g., spin-coating, drop-coating, or fiber-pulling methods for emerging components required in high-bit-rate communication channels, such as phosphor for microLEDs [22] and luminescent fibers for photodetection [4], [23].

In this work, we fundamentally investigated and proposed the use of colloidal PbS QDs, emitting in the NIR region, as visible-to-NIR color-converting components to address the linkage between VLC and silica-based fiber-optic communication, while at the same time, suggesting a possible dual-function downlink and uplink transmission that is less visually destructive for human vision in future optical-IoT systems. The material and optical properties of the solution-processed PbS QDs, e.g., absorption spectrum, photoluminescence (PL) spectrum, photoluminescence quantum yield (PLQY), high-resolution transmission electron microscopy (HRTEM) images, X-ray photoelectron spectroscopy (XPS) spectrum, and X-ray diffraction (XRD) spectrum were presented. A self-assembled visible-to-NIR communication system utilizing a 405-nm laser diode as the transmitter and an InGaAs-based photodetector as the photoreceiver, was also established in order to evaluate the feasibility of PbS QDs as color-conversion components for fiber-based optical communication links. The proposed color-conversion scheme was evaluated based on the power-efficient and more resilient orthogonal frequency-division multiplexing (OFDM) modulation scheme. Paving the way towards the era of optical-IoT systems, we envisaged that this first-of-its-kind and proof-of-principle demonstration paves a way towards realizing the aforementioned color-conversion components required in the visible-to-NIR optical communication links, while the use of solution-processed QDs obviates the need for cost- and process-intensive fabrication processes in extending the detection spectral range of current InGaAs-based photodetectors.

2. Material Synthesis and Preparation

The PbS QDs were synthesized using a conventional method reported previously [24]. The synthesis proceeded in Ar gas by using the Schlenk line. Lead oxide (0.446 g), oleic acid (3.8 mL) and ODE (50 mL) were mixed in a three-neck flask. The experiment requires multiple vacuums to drain water and oxygen from the flask. The reaction temperature rises to 150°C to form a pale-yellow lead oleate solution. Then the solution was pumped at 100°C for 2 hours. The solution of 90 μL hexamethyldisilane ($(TMS)_2S$) in 3 mL ODE was injected rapidly, and the color turned dark in several seconds. The reaction would continue for 8 minutes, and two other solutions (25 μL $(TMS)_2S$ in 3 mL ODE for each) were injected every 8 minutes. The reaction was quenched by an ice-bath and hexane. Acetone is added to precipitate the QDs.

3. Results and Discussion

3.1 Optical and Structural Characterization

The synthesized QDs powder was re-dispersed in octane and the QDs-octane solution was then sealed in a quartz cuvette. Fig. 2(a) and (b) show the absorbance/emission spectra and the time-resolved PL (TRPL) of the PbS QDs-octane solution, respectively. As shown in Fig. 2(a), the absorbance spectrum demonstrated high absorption towards the visible wavelength region, thus elucidating its potential for broadband yet efficient photoconversion from a shorter wavelength to a longer wavelength in the NIR region which matches the responsivity of intended InGaAs photodetectors. The emission peak of the sample is observed to be located at 1300 nm based on the optical excitation at 920 nm. In addition, a sharp absorption peak located at 1200 nm is originated from the PbS QDs [25], [26], while another absorption peak at 1400 nm is attributed
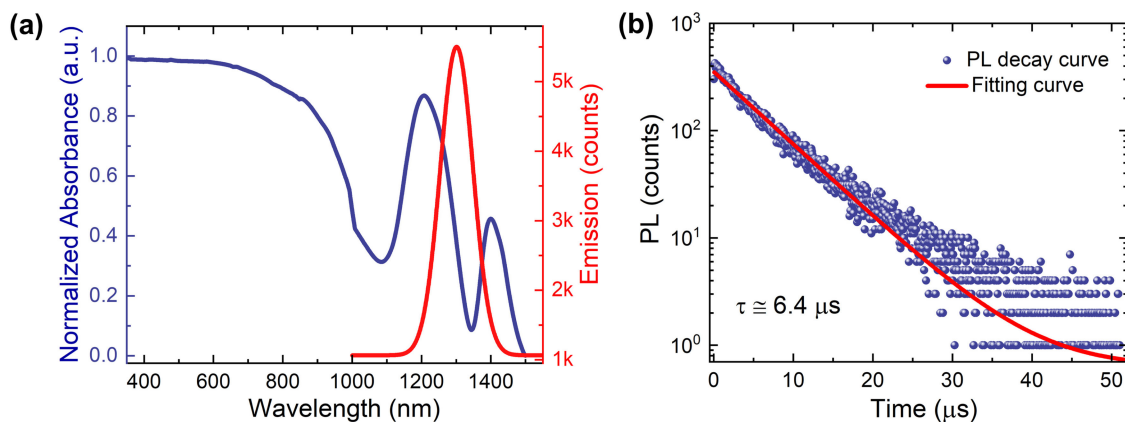
Fig. 2. (a) Normalized absorbance and PL emission, and (b) time-resolved PL measurement and single exponential decay fitting of PbS QDs.

to the OA ligands on the surfaces of PbS QDs, which are used to protect the PbS QDs from degradation and aggregation. The PLQY of the sample used in the experiment was measured to be about 88%. The steady state PL and PLQY measurements are performed by a fluorescence spectrometer (Edinburgh Instruments, F900). The absorption (A) spectrum was calculated by measuring the spectral transmittance (T) and reflectance (R) on the UV-VIS spectrometer and applying power continuity equation, i.e., $A = 1 - T - R$. The decay time was determined by the time-correlated single-photon counting (TCSPC) technique using a spectrofluorometer (Horiba, Fluorolog-3 Spectrofluorometer) with a 669-nm laser pulse. As shown in Fig. 2(b), the measured TRPL signal is then fitted with a single exponential decay function with an estimated time constant (τ) of about 6.4 μs.

The HRTEM image (see Fig. 3(a)) is acquired by an FEI Talos F200S microscope with an acceleration voltage of 200 kV. A well distributed size of PbS QDs could be observed. The particle sizes (diameter) shows a Gaussian distribution exhibiting a good quality of synthesized PbS QDs with an average size of 5.11 nm (see Fig. 3(b)). Then, the QDs are deposited on a silicon wafer for composition analysis based on XPS and XRD. The XPS result is acquired through a Thermo Fisher Scientific K-Alpha instrument. The four peaks corresponding to O, C, Pb, and S, have been indicated in Fig. 3(c), respectively. Detailed atomic percentages are provided in the inset table of Fig. 3(c). A large amount of OA ligands on the PbS QD surface contributes to the high O and C signals. Pb and S are also detected with an atomic ratio of 1.25:1. It is noted that the overdosed Pb precursor during the fabrication process constitute to the Pb-rich PbS QDs with Pb ion filling the outer surface. On the other hand, the existence of the (111) surface allows the PbS QDs to be mostly Pb-rich regardless of the sizes [27]. PbS QDs with this structure could provide more possible attachment points for OA ligands, which could increase the stability of PbS QDs. Moreover, the XRD analysis was performed based on Rigaku Smartlab to analyze the crystallization of PbS QDs. As shown in Fig. 3(d), three different crystal faces have been detected due to the different stacking direction of PbS QDs on the silicon wafer.

3.2 Color-conversion and Communication Setup

The as-synthesized PbS powder was re-dispersed in octane (10 mg/mL) under a nitrogen atmosphere. The sample was then placed in a quartz container. The PbS QDs-octane solution was then sealed with a rubber stopper and parafilm to protect the sample from oxidation, as shown in Fig. 4(a). The prepared sample is inserted into an integrating sphere (Thorlabs, IS236A-4). A 405-nm laser diode (LD) (SaNoor Technologies, SNLDP03) is used to excite the sample, as illustrated in Fig. 4(b). To receive the re-emitted signal from the PbS QDs, a fiber collimating

(a)

(b)

(c)

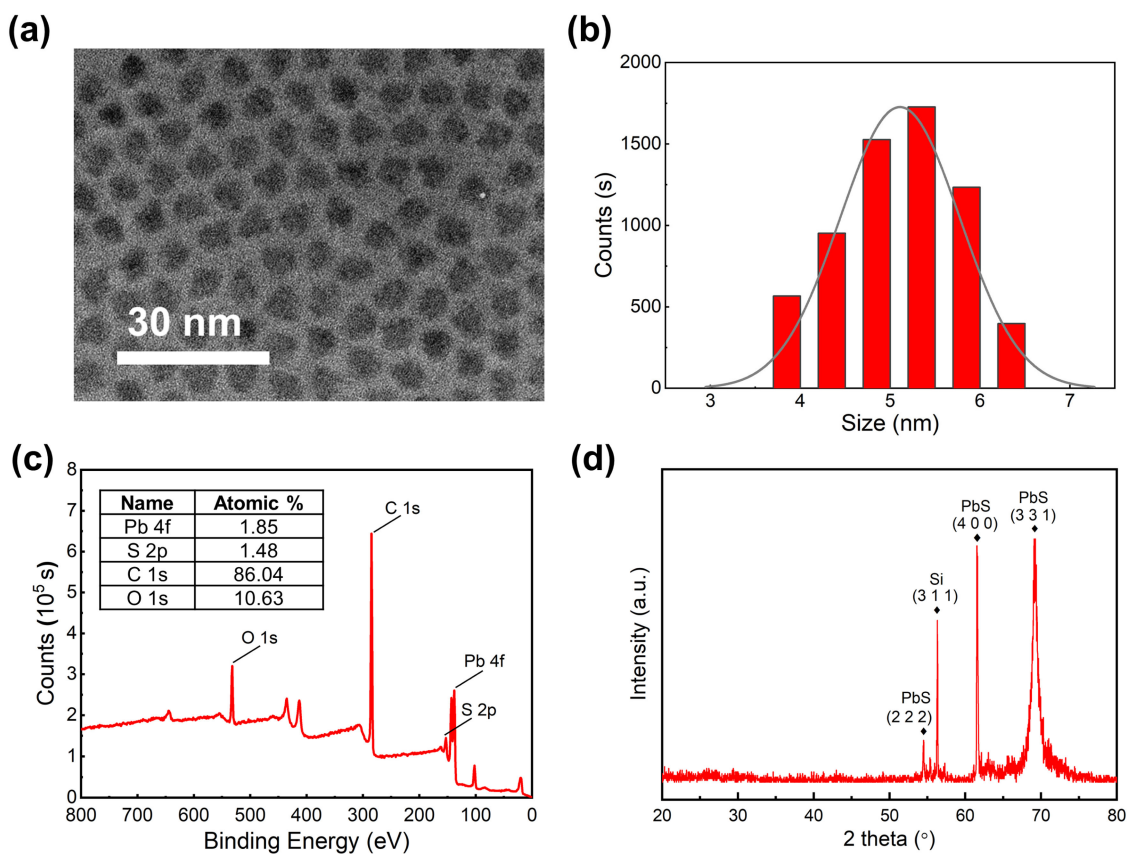| Name	Atomic %
Pb 4f	1.85
S 2p	1.48
C 1s	86.04
O 1s	10.63

(d)

Fig. 3. (a) HRTEM image of as-synthesized PbS QDs with the corresponding (b) average size distribution. (c) XPS spectrum of the QDs. The inset table shows the atomic percentage corresponding to the four main peaks. (d) XRD spectrum of PbS QDs deposited on a silicon wafer.

(a)

(b)

Collimating lens

405-nm laser diode

Optical fiber

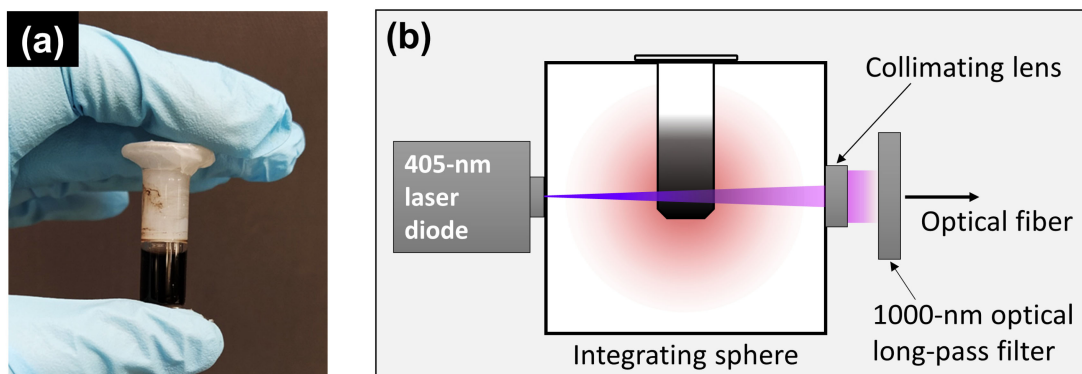1000-nm optical long-pass filter

Integrating sphere

Fig. 4. (a) Photograph image of PbS QDs-octane solution sample inside a quartz container. (b) Schematic diagram showing the 405-nm laser diode illuminating the quartz container housing the PbS QDs solution. The converted signal is coupled into the silica fiber through a collimating lens and a 1000-nm optical long-pass filter.
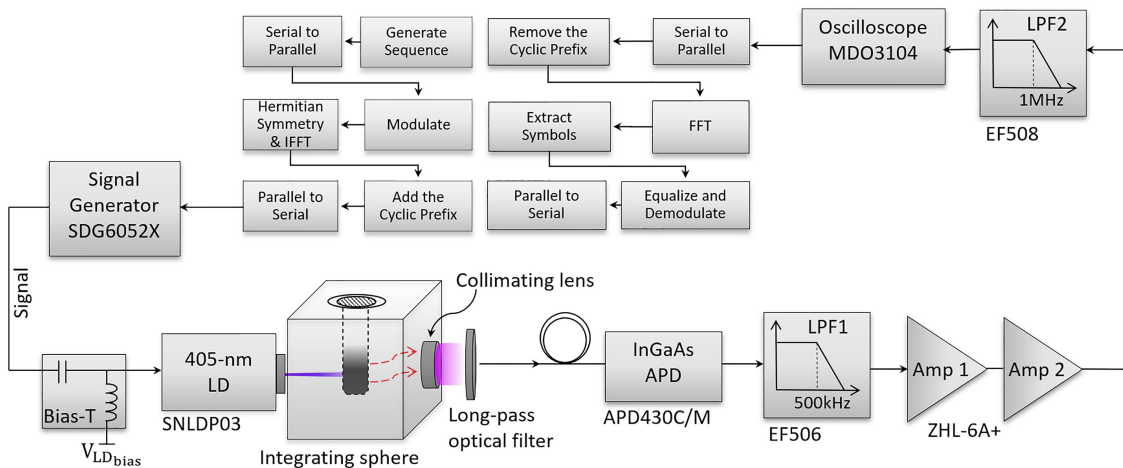
Fig. 5. Detailed block diagram of the established communication link with summarized OFDM modulation/demodulation steps.

lens (Thorlabs, F230FC-C-1310 nm) was mounted on the exit port of the integrating sphere. A 1000-nm long-pass filter (Thorlabs, FELH1000) was also used to remove any unabsorbed or stray photons coming directly from the excitation source. The modulated laser beam excites the PbS QDs-octane solution placed inside an integrating sphere which feeds the collected light into a silica optical fiber with a core diameter of 400 μm through the long-pass optical filter. The fiber is then mounted directly onto an InGaAs-based avalanche photodetector (Thorlabs, APD430C/M), where the detected signal is recorded using a mixed-domain oscilloscope (Tektronix, MDO3104) for offline processing on MATLAB. A bias-tee (Tektronix, PSPL5580) is used to combine the modulation signal with the direct-current (DC) bias driving the 405-nm LD. The modulation bandwidth of the system was measured by testing the frequency response. Based on the measurement, a frequency range from 50 to 250 kHz was utilized. To extend the usable bandwidth, an external circuit is attached to the bias-tee to further reduce the lower cut-off frequency from 100 kHz to 10 kHz. The detailed color conversion and signal acquisition schemes based on the OFDM modulation scheme are represented on the block diagrams in Fig. 5 and subsequent sections.

3.3 Signal Acquisition Scheme

The electrical current signal collected from the InGaAs-based APD is amplified internally by a low noise pre-amplifier which is integrated into the APD block. The detector multiplication factor, M, was set to the maximum value (M = 20) in order to maximize the power of the signal of interest. Due to the fact that the APD has a wide-bandwidth transfer characteristics with a −3-dB frequency at 400 MHz and the fact that the signal bandwidth is from 50 to 250 kHz, a passive RC low-pass filter (RC-LPF) with a cutoff frequency at 500 kHz (Thorlabs, EF506) was used in order to eliminate the effect of wide-band noise at the high-frequency band and to improve the sensitivity of the system. Two amplifying stages were employed to amplify the signal. The amplifiers (Mini-Circuits, ZHL-6A+) used in the experiment are internally stabilized and designed for high-frequency applications with a cutoff bandwidth at 500 MHz and with a gain of 24 dB. Furthermore, considering the fact that the most significant noise was originated from the amplifying stages, another RC-LPF with a 1-MHz cutoff was added in order to limit the bandwidth of the amplifiers.

3.4 Communication Performance Based on Orthogonal Frequency-Division Multiplexing

To improve the efficiency of the communication link, we implemented OFDM with adaptive data loading, which includes bit- and power-loading. This is done by first sending a test OFDM signal
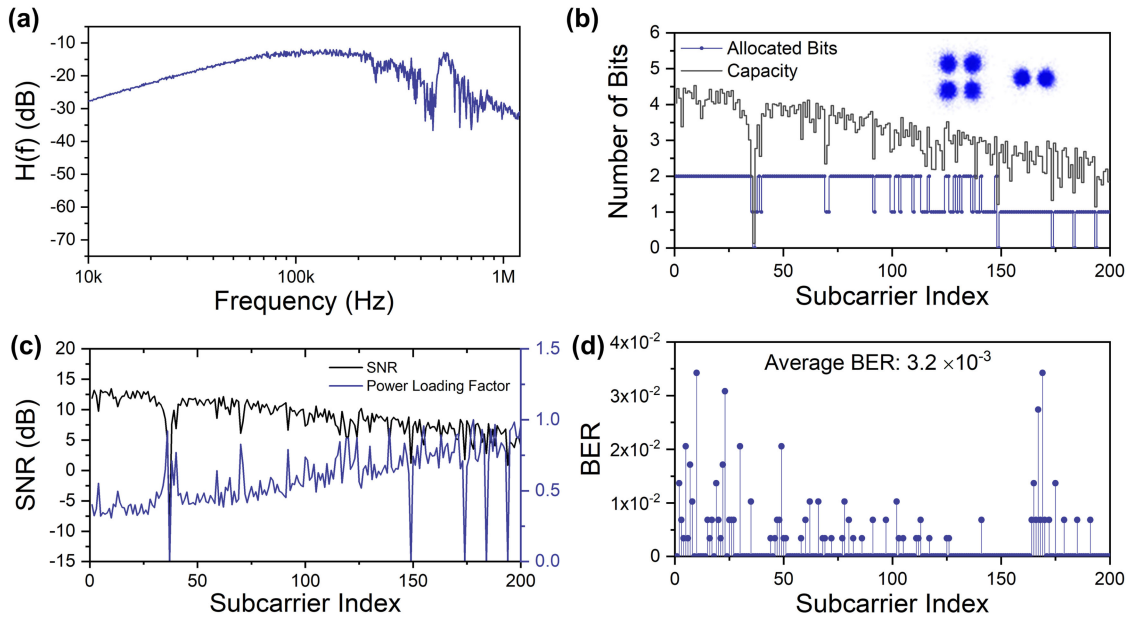
Fig. 6. (a) Communication link transfer characteristics. (b) The channel capacity and the allocated number of bits for each subcarrier as well as the received constellations. (c) The SNR of each subcarrier and the power loading factor. (d) The BER for each subcarrier.

based on 2-quadrature amplitude modulation (2-QAM) using the standard OFDM steps shown in Fig. 5. A pseudorandom binary sequence (PRBS) is generated and is then converted from serial to parallel. After that, the 2-QAM modulation is carried out. To make sure the generated signal can be used in intensity modulation of the laser, Hermitian symmetry is imposed to ensure that the output of the inverse fast Fourier transform (IFFT) is real-valued. In other words:

$$X_0(n) = X_{N_{FFT}/2}(n) = 0, \tag{1}$$

and

$$X_{N_{FFT}-k}(n) = X_k^*(n), \tag{2}$$

where $X_k(n)$ is the QAM symbol on the kth subcarrier in the nth OFDM symbol and $N_{FFT} = 1024$ is the size of the IFFT. This OFDM scheme is suitable for and has been demonstrated in both wireless channels and multimode fibers [28].

The low frequency subcarriers (50 subcarriers corresponding to around 49 kHz) are set to zero to avoid the baseline drift of electronic components and the low bandwidth response of the QDs at low frequencies, as shown in Fig. 6(a). Following the IFFT, a cyclic prefix is added after each OFDM symbol. The formed array of $N_S = 150$ OFDM symbols is converted to a serial sequence and is sent through the channel using the arbitrary waveform generator (AWG) with a sampling frequency, f_{AWG}, of 1 MSample/s. After the detector receives the signal, it is recorded using an oscilloscope with a sampling frequency of 5 MSample/s. The first step in the offline processing is to resample down to the sampling frequency of the AWG and synchronize the received signal using the known training symbols. The cyclic prefix is removed after converting the serial sequence to parallel. After performing the FFT and removing the Hermitian symmetry symbols, the symbols are post-equalized using a single-tap equalizer based on the training symbols (e.g., four symbols are used in this test). The symbols are then demodulated, and the bits are converted to a serial sequence for comparison and to calculate the bit error ratio (BER).

Based on the received 2-QAM test signal, the signal-to-noise ratio (SNR) is estimated based on the error vector magnitude (EVM). This is done by dividing the square of the magnitude of

TABLE 1
Comparison of Color-Conversion Method for Optical Communication Link
Based on Different Material System

Material	PLQY	−3 dB phosphor bandwidth	Signal wavelength of interest	Data rate (Modulation scheme)	Ref.
$CsPbBr_3$	70%	491 MHz	450 nm	2 Gbit/s (NRZ-OOK)	[19]
Carbon dots	21%	285 MHz	450 nm	350 Mbit/s (NRZ-OOK)	[33]
$CsPbBr_{1.8}I_{1.2}$	78%	73 MHz	445 nm	190 Mbit/s (NRZ-OOK)	[34]
$CsPbBr_3$	73%	70.92 MHz	278 nm	34 Mbit/s (NRZ-OOK)	[20]
PbS	88%	250 kHz	405 nm (Downlink), 1300 nm (Uplink)	0.27 Mbit/s (*M*-QAM OFDM)	The present work

the transmitted position on the constellation map by the square of the magnitude of the difference vector between the received position on the constellation map and the transmitted position. After repeating that for all symbols, the average SNR for each subcarrier is obtained. Based on the SNR, the number of bits allocated is determined and each subcarrier is given a factor to adjust its power to optimize the performance. The number of bits depends on the channel capacity as shown in Fig. 6(b), while Fig. 6(c) shows the power loading factors and the estimated SNR for each subcarrier. The channel capacity, C, can be estimated from the Shannon limit as shown in (3):

$$C = \log_2 (1 + \text{SNR}) \tag{3}$$

For subcarriers with SNRs below 3 dB, no bits are allocated. To calculate the overall data rate of the communication link, we employed (4) as shown below:

$$\text{Data Rate} = \frac{f_{\text{AWG}}}{N_{\text{FFT}} + N_{\text{CP}}} \sum_{k=1}^{N_{\text{SC}}} \log_2 (M_k) \tag{4}$$

where $N_{CP} = 10$ is the length of the cyclic prefix, $N_{SC} = 200$ is the number of subcarriers used, $M_k = 2^b$ is the QAM order of the kth subcarrier, and b is the number of bits allocated. Based on the bit loading scheme implemented, a data rate of 0.3 Mbit/s was achieved with an average BER of 3.2×10^{-3}. This BER is below the 7%-overhead forward error correction (FEC) BER limit of 3.8×10^{-3}. Fig. 6(d) shows the BER for each subcarrier. Assuming a 7% FEC overhead, and accounting for the 2.67% training symbols used for post equalization and synchronization, the net data rate can be estimated to be around 0.27 Mbit/s.

The modulation bandwidth of the OFDM modulation was chosen as 50 − 250 kHz in order to comply with the frequency response of the communication link. The actual frequency response of the experimental setup was mainly limited by the color-conversion stage with a −3-dB upper limit at about 250 kHz and the lower limit at about 70 kHz, as observed from the frequency response, H(f), where f is the frequency, in Fig. 6(a). Thus, the higher bandwidth-limit bottleneck was identified to be due to the PL recombination lifetime of the QDs, and it is possibly originated from the long-chain ligands used in this work that created multiple trap states [15]. The improvement in the radiative recombination lifetime in PbS QDs is nevertheless possible by modifying the surface ligand exchange of PbS QDs from long-chain ligands to shorter molecules as reported previously in [15], [29], where radiative recombination lifetime of down to few tens of ns could be realized. This would be ideal for realizing high-speed optical communication links. However, as compared to halide-perovskite-based quantum dots, which typically exhibit a fast recombination lifetime of less than 10 ns [19], [20], [30], significant improvement in material synthesis is required to minimize non-radiative recombination centers or intermediate trap states. Moreover, the reported data rate can be readily used in various optical-IoT applications, including wearables, smart appliances, health monitoring, and industrial IoT [31], [32]. Another aspect that could have degraded the

frequency response of the system is the optical coupling loss that occurred at the point where the optical signal is guided into a silica-based fiber from the integrating sphere. The optical signal escaping from the integrating sphere was collimated with the collimating lens with an output beam diameter of about 0.8 mm, whereas the silica fiber core diameter is only about 400 μm. The further improvement in fiber coupling losses would increase SNR performance of the system, and would allow higher modulation orders with bit- and/or power-loading schemes to be applied in order to realize over Mbit/s data transmission. Table 1 summarizes the reported color-conversion method for transceiver units in optical-based communication links based on different QDs/nanocrystals materials, as well as the maximum reported data rate.

4. Conclusion

In this work, we have demonstrated the first-of-its-kind and proof-of-principle system using PbS QDs as visible-to-near-infrared conversion materials for a 0.27-Mbits/s OFDM-based optical communication link. The data rate in the range of sub-Mbit/s is sufficient to enable eye-safe remote access control over a vast majority of optical-IoT devices in an indoor environment. Furthermore, the use of PbS QDs as the intermediate medium can extend the detection range of matured InGaAs-based photodetectors, as well as potentially serve the dual-function of downlink and uplink transmission for various optical-IoT systems. Through additional ligands passivation or external polymer passivation, this work also further paves the way to realize future solution-processed and flexible QDs-based components that are suitable for system integration. Some examples include polymer-based luminescent fibers photoreceivers, polymer-based QDs receivers and QDs-doped glass fibers, which inherently exhibit large detection spectral range covering the visible-to-near-infrared region, as well as potentially suitable for further integration with silica-based waveguides in photonic integrated circuits.

Acknowledgment

References

[1] H. Haas, "LiFi is a paradigm-shifting 5G technology," *Rev. Phys.*, vol. 3, pp. 26–31, 2018.
[2] H. Haas *et al.*, "Introduction to indoor networking concepts and challenges in LiFi," *J. Opt. Commun. Netw.*, vol. 12, no. 2, pp. A190–A203, 2020.
[3] M. Z. Chowdhury, M. T. Hossan, A. Islam, and Y. M. Jang, "A comparative survey of optical wireless technologies: Architectures and applications," *IEEE Access*, vol. 6, pp. 9819–9840, 2018.
[4] T. Peyronel, K. J. Quirk, S. C. Wang, and T. G. Tiecke, "Luminescent detector for free-space optical communication," *Optica*, vol. 3, no. 7, pp. 787, 2016.
[5] Y. Dong *et al.*, "Nanopatterned luminescent concentrators for visible light communications," *Opt. Exp.*, vol. 25, no. 18, 2017, Art. no. 21926.
[6] P. P. Manousiadis *et al.*, "Wide field-of-view fluorescent antenna for visible light communications beyond the étendue limit," *Optica*, vol. 3, no. 7, pp. 702–706, 2016.
[7] E. F. Schubert, *Light-emitting Diodes*. Cambridge, U.K.: Cambridge Univ. Press, 2003.
[8] G. Stepniak, M. Schüppert, and C. A. Bunge, "Polymer-optical fibres for data transmission," in *Polymer Optical Fibres: Fibre Types, Materials, Fabrication, Characterisation and Applications*, 2017, pp. 217–310.
[9] G. Keiser, "Optical Fiber Communications," in *Wiley Encyclopedia of Telecommunications*. 2003, doi: org/10.1002/0471219282.eot158.
[10] D. M. Geum *et al.*, "Monolithic integration of visible GaAs and near-infrared InGaAs for multicolor photodetectors by using high-throughput epitaxial lift-off toward high-resolution imaging systems," *Sci. Rep.*, vol. 9, no. 1, pp. 1–12, 2019.
[11] P. Wang *et al.*, "Arrayed van der waals broadband detectors for dual-band detection," *Adv. Mater.*, vol. 29, no. 16, pp. 1–8, 2017.
[12] L. Li, Z. Lou, and G. Shen, "Flexible broadband image sensors with SnS quantum dots/Zn$_2$SnO$_4$ nanowires hybrid nanostructures," *Adv. Funct. Mater.*, vol. 28, no. 6, pp. 1–10, 2018.
[13] M. I. Bodnarchuk and M. V. Kovalenko, *Engineering Colloidal Quantum Dots*. Cambridge, U.K.: Cambridge Univ. Press, 2013.

[14] H. Tang, J. Zhong, K. Wang, and X. W. Sun, "11-2: Methylammonium iodide (MAI) enhanced, solution processed high-performance photodetector based on lead sulfide quantum dots," *SID Symp. Dig. Tech. Pap.*, vol. 49, no. 1, pp. 108–111, 2018.

[15] H. Tang *et al.*, "Lead sulfide quantum dot photodetector with enhanced responsivity through a two-step ligand-exchange method," *ACS Appl. Nano Mater.*, vol. 2, no. 10, pp. 6135–6143, 2019.

[16] T. K. Ng *et al.*, "Group-III-nitride and halide-perovskite semiconductor gain media for amplified spontaneous emission and lasing applications," *J. Phys. D. Appl. Phys.*, vol. 54, no. 14, 2021, Art. no. 143001.

[17] Y. Shirasaki, G. J. Supran, M. G. Bawendi, and V. Bulović, "Emergence of colloidal quantum-dot light-emitting technologies," *Nat. Photon.*, vol. 7, no. 1, pp. 13–23, 2013.

[18] S. A. Mcdonald *et al.*, "Solution-processed PbS quantum dot infrared photodetectors and photovoltaics," *Nat. Mater.*, vol. 4, no. 2, pp. 138–142, 2005.

[19] I. Dursun *et al.*, "Perovskite nanocrystals as a color converter for visible light communication," *ACS Photon.*, vol. 3, no. 7, pp. 1150–1156, 2016.

[20] C. H. Kang *et al.*, "High-speed colour-converting photodetector with all-inorganic $CsPbBr_3$ perovskite nanocrystals for ultraviolet light communication," *Light Sci. Appl.*, vol. 8, no. 1, pp. 94, 2019.

[21] Y. Choi, S. Sim, S. C. Lim, Y. H. Lee, and H. Choi, "Ultrafast biexciton spectroscopy in semiconductor quantum dots: Evidence for early emergence of multiple-exciton generation," *Sci. Rep.*, vol. 3, pp. 1–6, 2013.

[22] K. Rae *et al.*, "InGaN μLEDs integrated onto colloidal quantum dot functionalized ultra-thin glass," *Opt. Exp.*, vol. 25, no. 16, 2017, Art. no. 19179.

[23] C. H. Kang *et al.*, "Ultraviolet-to-blue color-converting scintillating-fibers photoreceiver for 375-nm laser-based under-water wireless optical communication," *Opt. Exp.*, vol. 27, no. 21, 2019, Art. no. 30450.

[24] J. W. Lee, D. Y. Kim, S. Baek, H. Yu, and F. So, "Inorganic UV-visible-SWIR broadband photodetector based on monodisperse PbS nanocrystals," *Small*, vol. 12, no. 10, pp. 1328–1333, 2016.

[25] H. Fu and S. W. Tsang, "Infrared colloidal lead chalcogenide nanocrystals: Synthesis, properties, and photovoltaic applications," *Nanoscale*, vol. 4, no. 7, pp. 2187–2201, 2012.

[26] G. Su, C. Liu, Z. Deng, X. Zhao, and X. Zhou, "Size-dependent photoluminescence of PbS QDs embedded in silicate glasses," *Opt. Mater. Exp.*, vol. 7, no. 7, pp. 2194–2207, 2017.

[27] H. Choi, J. H. Ko, Y. H. Kim, and S. Jeong, "Steric-hindrance-driven shape transition in PbS quantum dots: Under-standing size-dependent stability," *J. Amer. Chem. Soc.*, vol. 135, no. 14, pp. 5278–5281, 2013.

[28] J. Armstrong, "OFDM for optical communications," *J. Light. Technol.*, vol. 27, no. 3, pp. 189–204, 2009.

[29] S. Kahmann, A. Mura, L. Protesescu, M. V. Kovalenko, C. J. Brabec, and M. A. Loi, "Opto-electronics of PbS quantum dot and narrow bandgap polymer blends," *J. Mater. Chem. C*, vol. 3, no. 21, pp. 5499–5505, 2015.

[30] J. Almutlaq *et al.*, "$CsMnBr_3$: Lead-Free Nanocrystals with High Photoluminescence Quantum Yield and Picosecond Radiative Lifetime," *ACS Mater. Lett.,* pp. 290–297, 2021.

[31] AT&T. "What you need to know about IoT wide area networks," 2016. [Online]. Available: https://www.itu.int/dms_pub/itu-r/md/16/rsg1sg5iot16/inf/R16-RSG1SG5IOT16-INF-0011!N2!PDF-E.pdf

[32] A. Lasku, H. Pichai, R. A. Wadman, and S. McDevitt, "Realizing the potential of the Internet of Things with 5G," *Prism*, 2020. [Online]. Available: https://www.adlittle.com/en/IoTpotential5G#:~:text=This%20is%20set%20to%20change,1.5%20trillion%20by%2020301

[33] Z. Zhou *et al.*, "Hydrogen peroxide-treated carbon dot phosphor with a bathochromic-shifted, aggregation-enhanced emission for light-emitting devices and visible light communication," *Adv. Sci.*, vol. 5, no. 8, 2018, Art. no. 1800369.

[34] S. Mei *et al.*, "High-bandwidth white-light system combining a micro-LED with perovskite quantum dots for visible light communication," *ACS Appl. Mater. Interfaces*, vol. 10, no. 6, pp. 5641–5648, 2018.